



**HAL**  
open science

# Bayesian dual inversion of experimental telescope acceptance and integrated flux for geophysical muon tomography

N. Lesparre, D. Gibert, J. Marteau

► **To cite this version:**

N. Lesparre, D. Gibert, J. Marteau. Bayesian dual inversion of experimental telescope acceptance and integrated flux for geophysical muon tomography. *Geophysical Journal International*, 2012, 188, pp.490-497. 10.1111/j.1365-246X.2011.05268.x . in2p3-00666938

**HAL Id: in2p3-00666938**

**<https://hal.in2p3.fr/in2p3-00666938>**

Submitted on 19 May 2017

**HAL** is a multi-disciplinary open access archive for the deposit and dissemination of scientific research documents, whether they are published or not. The documents may come from teaching and research institutions in France or abroad, or from public or private research centers.

L'archive ouverte pluridisciplinaire **HAL**, est destinée au dépôt et à la diffusion de documents scientifiques de niveau recherche, publiés ou non, émanant des établissements d'enseignement et de recherche français ou étrangers, des laboratoires publics ou privés.

# Bayesian dual inversion of experimental telescope acceptance and integrated flux for geophysical muon tomography

Nolwenn Lesparre,<sup>1</sup> Dominique Gibert<sup>1</sup> and Jacques Marteau<sup>2</sup>

<sup>1</sup>Institut de Physique du Globe de Paris (UMR CNRS 7154), Sorbonne Paris Cité, Paris, France. E-mail: gibert@univ-rennes1.fr

<sup>2</sup>Institut de Physique Nucléaire de Lyon (UMR CNRS 5822), Lyon, France

Accepted 2011 October 17. Received 2011 September 1; in original form 2011 March 26

## SUMMARY

Density tomography of rock volumes with cosmic muons involves telescopes equipped with pixelized matrices of scintillator strips able to simultaneously measure the flux of muons in hundredths of directions. The resulting muon radiography images are a measure of the amount of matter integrated along each line of sight inside the geological target. This information constitutes the primary data at the root of muon density 3-D tomography. Before being used for either interpretation or tomography inversion, the radiographies must be corrected from artefacts due to imperfect detection capacity of the detection matrices. We present a correction method based on a Bayesian inversion to construct a probabilistic model of the distorted telescope acceptance from which undistorted radiographies may be obtained. The method also allows to simultaneously derive a stochastic model for the incident flux of muons. The resulting non-linear inverse problem is solved with the Metropolis-annealing algorithm, which allows to easily implement symmetry constraints to reduce the non-uniqueness. An inversion of real data acquired with one of our field muon telescopes is presented and discussed.

**Key words:** Inverse theory; Tomography; Probability distributions; Instrumental noise.

## 1 INTRODUCTION

The objective of muon tomography is to determine the density of large volumes of rock by using the attenuation of the flux of cosmic muons crossing the geological body of interest (e.g. Nagamine 2003). The small cross-section of muons (Barrett 1952) and their energy range in the secondary cosmic ray spectrum (Gaisser & Stanev 2008) allow to probe geological objects at subkilometre scales. Muon tomography presently benefits from a growing interest since the pioneering studies by Nagamine (1995) and Nagamine *et al.* (1995). These studies were soon followed by others to image spatial and temporal variations of the density inside volcanoes (Tanaka *et al.* 2008, Tanaka *et al.* 2009a,b and references therein).

In this paper, we shall consider the case where muons flux is measured by so-called ‘telescopes’ made of scintillator matrices as shown in Fig. 1 (Marteau *et al.* 2011). Each matrix is composed of  $N_x$  horizontal and  $N_y$  vertical scintillator strips whose intersections define pixels. The detected muon trajectory is determined by the pair of pixels  $(a_{i,j}, b_{k,l})$  fired by the particle, where  $a_{i,j}$  is a pixel belonging to matrix  $A$  and  $b_{k,l}$  belongs to matrix  $B$ . Such a pair of matrices defines a set of  $(2N_x - 1) \times (2N_y - 1)$  discrete directions  $\mathbf{r}_{m,n}$ , where the indices  $m = i - k$  and  $n = j - l$  only depend on the relative shift between the  $a_{i,j}$  and  $b_{k,l}$  pixels.

In practice, the muon count  $\nu$ , detected by the telescope in a given direction,  $\mathbf{r}_{m,n}$ , directly depends on the telescope acceptance,  $T$ , expressed in  $\text{cm}^2 \text{sr}$ .  $T$  quantifies the telescope capability to

measure a flux coming in a given solid angle centred in a given direction.  $\nu$  reads

$$\nu(\mathbf{r}_{m,n}, \Delta T) = I(\mathbf{r}_{m,n}) \times \Delta T \times T(\mathbf{r}_{m,n}), \quad (1)$$

where  $I$  is the muons flux in  $\text{cm}^{-2} \text{sr}^{-1} \text{s}^{-1}$ , and  $\Delta T$  is the measurement duration obtained by the feasibility formula as established by Lesparre *et al.* (2010). The acceptance may be written as

$$T(\mathbf{r}_{m,n}) = S(\mathbf{r}_{m,n}) \times \delta\Omega(\mathbf{r}_{m,n}). \quad (2)$$

The detection surface  $S$  is given by the pixels size  $d$  and number  $N_x \times N_y$ , in a matrix, and the angular aperture  $\delta\Omega$  depends on the distance  $D$  between the matrices. Fig. 2 shows the angular aperture and the acceptance for the 961 discrete directions  $\mathbf{r}_{m,n}$  of a telescope as shown in Fig. 1 with  $N_x = N_y = 16$ ,  $d = 5 \text{ cm}$  and  $D = 115 \text{ cm}$ . As expected, the acceptance is maximum for direction  $\mathbf{r}_{0,0}$ , perpendicular to the matrices since all pixels contribute to the detection surface. The acceptance is small for a margin corresponding to the directions, which most depart from  $\mathbf{r}_{0,0}$  and only a fraction of all possible directions of detection will be efficient in practice.

The quantity of interest is the integrated flux  $I$  to be compared with the flux obtained for the tomography models. Using eq. (1), we have

$$I(\mathbf{r}_{m,n}) = \frac{\nu(\mathbf{r}_{m,n}, \Delta T)}{\Delta T \times T(\mathbf{r}_{m,n})}, \quad (3)$$

which explicitly shows the importance of the acceptance function, appearing in the right-hand part denominator.

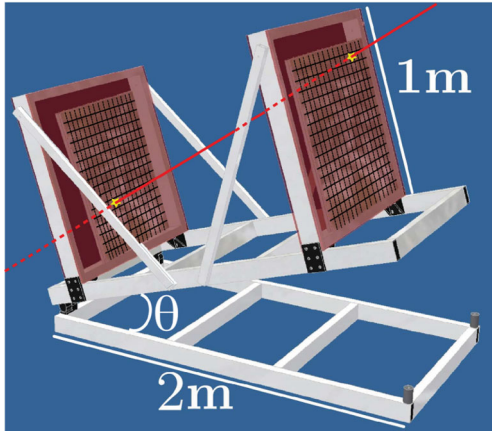


**Figure 1.** Schematic view of a muon telescope equipped with two  $16 \times 16$  pixels matrices.

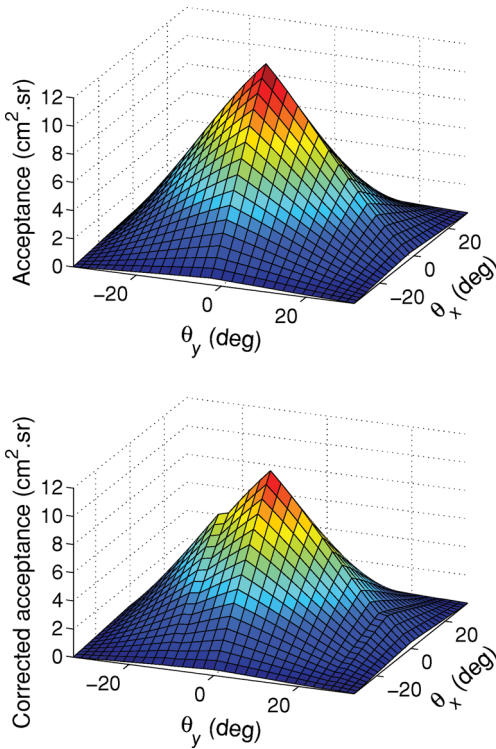


**Figure 2.** Angular properties of a two  $16 \times 16$  matrices telescope with pixel size  $d = 5$  cm and  $D = 115$  cm interdistance: (top panel) acceptance  $\mathcal{T}(\mathbf{r}_{m,n})$  for each discrete direction  $\mathbf{r}_{m,n}$  of the pair of matrices; (bottom panel) corrected acceptance with the malfunctioning bar  $Y_{12}$  (Fig. 3) removed from the computation.

Because of the power-law fall-off of the energy spectrum, the muons flux emerging from, say a volcano, is orders of magnitude lower than the flux measured in open-sky conditions. Also, the flux variations induced by tiny density heterogeneities inside the object of interest are small and may be blurred by defects in the acceptance function, a problem early recognized by Alvarez *et al.* (1970). A prior estimate of function  $\mathcal{T}$  may be obtained from purely geometrical consideration (Gibert *et al.* 2010; Lesparre *et al.* 2010). Despite its usefulness for preliminary modellings and design of field operations, this theoretical acceptance is far too inaccurate to determine the measured flux with eq. (3).

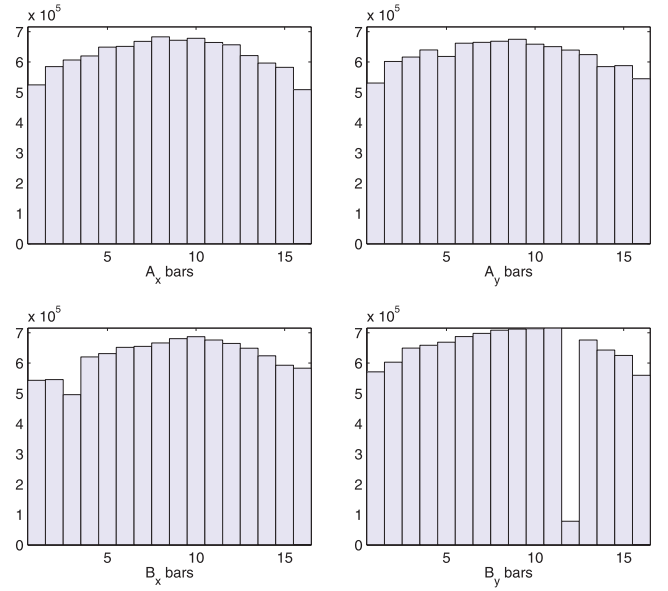


**Figure 3.** Events distribution detected on the front and rear  $X$  and  $Y$  planes of a telescope for the third data set of Table 1.

**Table 1.** Orientations and acquisition times of the data sets analysed.

Data set number	Zenith angle	Azimuth angle	Acquisition time (hr)
1	$61.4^\circ$	$72^\circ$	141
2	$47.2^\circ$	$72^\circ$	170
3	$1.35^\circ$	$45^\circ$	170

In this paper, we derive an inverse method to obtain the acceptance function of a telescope using a reference data set. The so-obtained acceptance relies on the determination of the bars efficiency forming the scintillator matrices and, consequently, accounts for eventual defects in the detection efficiency of these bars.

Before going into the details of the method, we briefly present an example of acceptance defect for telescope (Fig. 3), due to the bad optical coupling of the rear matrix  $Y_{12}$  channel. In this example, the telescope has been oriented in three different directions to measure the open-sky muon flux for zenith angles ranging from  $0^\circ$  to  $90^\circ$  and a total acquisition time of about 3 weeks (Table 1). The flux computed with the theoretical telescope acceptance (top part of Fig. 2) is shown on the top part of Fig. 4. This flux varies principally with the zenith angle from  $1 \times 10^{-4} \text{ cm}^{-2} \text{ sr}^{-1} \text{ s}^{-1}$  to  $8.5 \times 10^{-3} \text{ cm}^{-2} \text{ sr}^{-1} \text{ s}^{-1}$ , but one can observe several defects affecting the circular symmetry expected for the open-sky flux. These defects disappear (bottom part of Fig. 4) when accounting for the  $Y_{12}$  bar failure to compute the corrected acceptance shown in the bottom part of Fig. 2). The circular symmetry is recovered but some irregularities are still observed.

## 2 BAYESIAN INVERSION OF THE ACCEPTANCE-FLUX MODEL

### 2.1 Parametrization of the model

Both the acceptance and the integrated flux are fundamental unknowns of the muon tomography problem, and are inversely correlated quantities as shown in eq. (3). For this reason, we propose a

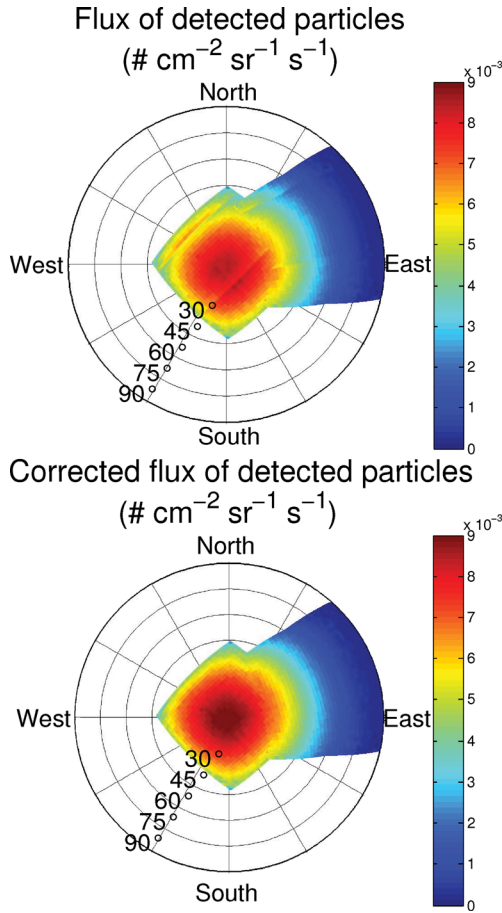


**Figure 4.** (Top panel) Detected flux: number of particles detected divided by the acquisition time and the theoretical telescope acceptance. (Bottom panel) Corrected flux of particles detected, computed with the acceptance on right part of Fig. 2.

simultaneous dual inversion of the integrated flux and the telescope acceptance.

In the example discussed earlier, the bar failure is considered as total, and the corrected acceptance was computed by simply removing the  $Y_{12}$  bar from the rear matrix model. However, in most cases, the deficiency of the bars is not evident and it is necessary to consider that the number of events detected by a given bar is only a fraction, hereafter called the efficiency, of the particles number which actually hit the bar.

Assuming a constant efficiency for each scintillator bar of a telescope, the number of muons  $v_{i,j,k,l}$  detected by a set of four bars [one  $(X, Y)$  pair for both the front and rear matrices] can be written as

$$v_{i,j,k,l} = a_i^x \times a_j^y \times b_k^x \times b_l^y \times n_{i,j,k,l}, \quad (4)$$

where  $a_i^x$  and  $a_j^y$ , respectively, represent the efficiencies of bars  $X_i$  and  $Y_j$  of the front matrix and  $b_k^x$  and  $b_l^y$  play the same role for the rear matrix. The efficiencies are real numbers belonging to the  $[0, 1]$  interval, and the number of  $a$  and  $b$  values to be determined equals  $2(N_x + N_y)$  (e.g. 64 for  $N_x = N_y = 16$ ). The  $n_{i,j,k,l}$  terms represent the unknown number of particles, which actually crossed the bars and are such that  $n_{i,j,k,l} \geq v_{i,j,k,l}$ . The number of  $n_{i,j,k,l}$  terms equals  $(N_x \times N_y)^2$  (e.g. 65 536 for  $N_x = N_y = 16$ ).

We assume that all  $n_{i,j,k,l}$  terms, such that  $i - k = m, j - l = n$ , and corresponding to the same direction  $\mathbf{r}_{m,n}$ , are realizations of the same Poissonian process  $\mathcal{P}$  with parameter  $\lambda_{m,n} > 0$ . Consequently,

the  $n_{i,j,k,l}$  terms are realizations of the generating  $\mathcal{P}$  process.

$$\mathcal{P}(\lambda_{m,n}) \mapsto \mathcal{N}_{m,n} \equiv \{n_{i,j,k,l} / i - k = m, j - l = n\}. \quad (5)$$

This equation shows that the elements of subset  $\mathcal{N}_{m,n}$  depend on a single parameter  $\lambda_{m,n}$ . Consequently the unknown parameters are no more the  $n_{i,j,k,l}$  terms but the  $\lambda_{m,n}$  terms instead, and the dimensionality of the parameter space is dramatically reduced from  $2(N_x + N_y) + (N_x \times N_y)^2$  to  $2(N_x + N_y) + (2N_x - 1) \times (2N_y - 1)$  (e.g. from 65 600 to 1025 for  $N_x = N_y = 16$ ). From underdetermined, the inverse problem becomes overdetermined.

Constraints tighter than the ones represented by eq. (5) could be put on the  $n_{i,j,k,l}$  terms by exploiting the fact that several directions  $\mathbf{r}$  may share the same Poissonian parameter  $\lambda$ . This is possible in particular instances where the measured integrated flux is supposed to satisfy some symmetry properties. For example, the open-sky flux shown in Fig. 4 has a circular symmetry, which could be used to further reduce the dimensionality of the parameter space, hence stabilizing the inverse problem. Such constrains are case dependent contrarily to the weak constrains of eq. (5), which hold in all situations. However, these specific constrains consist in equating some  $\lambda_{m,n}$  terms and merging the corresponding  $\mathcal{N}_{m,n}$ . The generic form of the resulting mapping reads

$$\mathcal{P}(\lambda_\alpha) \mapsto \mathcal{N}_\alpha \equiv \bigcup \mathcal{N}_{m,n}, \quad (6)$$

where the union symbol is understood to concern the  $\mathcal{N}_{m,n}$  whose elements are linked to the common  $\lambda_\alpha$ .

## 2.2 Derivation of the Bayesian posterior probability

We now formulate a Bayesian solution of eq. (4) accounting for all constraints discussed earlier. The posterior probability of the parameters reads

$$P(\mathbf{\Lambda}, \mathbf{e} | \mathbf{v}) = \frac{P(\mathbf{\Lambda}, \mathbf{e}) \times P(\mathbf{v} | \mathbf{\Lambda}, \mathbf{e})}{\int_{\mathbf{\Lambda}, \mathbf{e}} P(\mathbf{\Lambda}, \mathbf{e}) \times P(\mathbf{v} | \mathbf{\Lambda}, \mathbf{e})}, \quad (7)$$

where

$$\mathbf{v} = (v_{1,1,1,1} \cdots v_{i,j,k,l} \cdots v_{N_x, N_y, N_x, N_y})^t, \quad (8a)$$

$$\mathbf{\Lambda} = (\cdots \lambda_\alpha \cdots)^t, \quad (8b)$$

$$\mathbf{e} = (\mathbf{a} | \mathbf{b})^t, \quad (8c)$$

$$\mathbf{a} = (a_1^x \cdots a_{N_x}^x | a_1^y \cdots a_{N_y}^y)^t, \quad (8d)$$

$$\mathbf{b} = (b_1^x \cdots b_{N_x}^x | b_1^y \cdots b_{N_y}^y)^t. \quad (8e)$$

The vector  $\mathbf{v}$  is the data set, that is, a number of muons detected (see also eq. 4). Vectors  $\mathbf{\Lambda}$  and  $\mathbf{e}$  represent the unknown parameters to be determined.

The joined prior probability  $P(\mathbf{\Lambda}, \mathbf{e})$  may be rewritten as

$$P(\mathbf{\Lambda}, \mathbf{e}) = \prod_{\alpha} P(\lambda_\alpha) \times \prod_{\beta} P(e_\beta), \quad (9)$$

with (non-normalized)

$$P(\lambda_\alpha) = \begin{cases} 0 & \text{if } \lambda_\alpha \leq 0 \\ 1 & \text{if } \lambda_\alpha > 0 \end{cases}, \quad (10a)$$

$$P(e_\beta) = \begin{cases} 1 & \text{if } e_\beta \in (0, 1) \\ 0 & \text{otherwise.} \end{cases} \quad (10b)$$

The conditional probability  $P(\mathbf{v} | \mathbf{\Lambda}, \mathbf{e})$  may equally be rewritten as

$$P(\mathbf{v} | \mathbf{\Lambda}, \mathbf{e}) = \prod_{\text{all } v_{i,j,k,l}} P(v_{i,j,k,l} | \mathbf{\Lambda}, \mathbf{e}). \quad (11)$$

Accounting for the mapping of eq. (6) which assigns a unique  $\lambda_\alpha$  to the  $v$  terms of the  $\mathcal{N}_\alpha$  set, eq. (11) becomes

$$P(\mathbf{v} | \mathbf{\Lambda}, \mathbf{e}) = \prod_{\alpha} \prod_{v_{i,j,k,l} \in \mathcal{N}_\alpha} P(v_{i,j,k,l} | \lambda_\alpha, \mathbf{e}) \quad (12a)$$

$$= \prod_{\alpha} \prod_{v_{i,j,k,l} \in \mathcal{N}_\alpha} P(v_{i,j,k,l} | \mathcal{P}(\lambda_{\alpha,i,j,k,l})) \quad (12b)$$

$$= \prod_{\alpha} \prod_{v_{i,j,k,l} \in \mathcal{N}_\alpha} \exp(-\lambda_{\alpha,i,j,k,l}) \frac{v_{i,j,k,l}^{\lambda_{\alpha,i,j,k,l}}}{v_{i,j,k,l}!}, \quad (12c)$$

with the corrected Poissonian parameters defined as  $\lambda_{\alpha,i,j,k,l} \equiv a_i^\alpha b_j^\alpha b_k^\alpha b_l^\alpha \lambda_\alpha$ .

In eq. (12b) we introduce the Poissonian process and the probability resumes to the chance that  $v_{i,j,k,l}$  muons are detected under the condition that this number is supposed to be drawn from a Poissonian process with the corrected parameter  $\lambda_{\alpha,i,j,k,l}$ . For both  $v_{i,j,k,l}$  and  $\lambda_{\alpha,i,j,k,l}$  larger than 50, the Poissonian distribution may safely be replaced by the Gaussian with mean and variance  $\lambda_{\alpha,i,j,k,l}$  (Papoulis & Pillai 2002), and eq. (12c) becomes

$$P(\mathbf{v} | \mathbf{\Lambda}, \mathbf{e}) = \prod_{\alpha} \prod_{v_{i,j,k,l} \in \mathcal{N}_\alpha} \frac{\exp\left[-\frac{(v_{i,j,k,l} - \lambda_{\alpha,i,j,k,l})^2}{2\lambda_{\alpha,i,j,k,l}}\right]}{\sqrt{2\pi\lambda_{\alpha,i,j,k,l}}}. \quad (13)$$

The probability densities derived (see eqs 10a, 10b and 12c or 13) may now be inserted in eq. (7) to obtain the Bayesian solution of the inverse problem with unknown parameters  $\lambda_\alpha$  and  $e_\beta$ . Solving eq. (7) to obtain models with the highest posterior probability is a non-linear inverse problem as can be seen from either eq. (12c) or (13) (Tarantola, 2005). In the next section, we present the Metropolis-annealing method used to numerically solve the inverse problem.

### 3 METROPOLIS-ANNEALING NON-LINEAR INVERSION

#### 3.1 Presentation of the method

We now describe the Metropolis-annealing algorithm used to obtain the maximum likelihood solution of eq. (7) (Metropolis *et al.* 1953; Kirkpatrick *et al.* 1983; Bhanot 1988). This algorithm is a two-loop iterative procedure with the inner loop corresponding to a Metropolis stochastic relaxation and the outer one to an annealing anamorphosis of the posterior probability (eq. 7) to progressively guide the Markov Chain Monte Carlo sequence towards the maximum likelihood model. A great advantage of this approach is that the Metropolis algorithm does not need normalized probability densities, so that the unknown integral at the numerator of eq. (7) may be ignored. The reader interested in the details of the Metropolis-annealing non-linear inversion is referred to Gibert & Virieux (1991), Pessel & Gibert (2003), Gibert & Le Mouél (2008) and Nicollin *et al.* (2010) for applications in various fields of geophysics.

The Metropolis relaxation is a stochastic process producing a Markov Chain Monte Carlo sequence whose elements are asymptotically statistically distributed according to a given probability

density. The algorithm proceeds as a stochastic filter which issues the desired sequence of models from a white input series of models randomly chosen in the parameter space. In practice, the next model  $(\mathbf{\Lambda}, \mathbf{e})_{\gamma+1}$  is obtained by drawing a trial model,  $(\mathbf{\Lambda}, \mathbf{e})_{\text{TRY}}$ , and making the insertion in the Markov sequence according to the probability

$$P[(\mathbf{\Lambda}, \mathbf{e})_{\gamma+1} \leftarrow (\mathbf{\Lambda}, \mathbf{e})_{\text{TRY}}] = \min\left[\frac{P[(\mathbf{\Lambda}, \mathbf{e})_{\text{TRY}} | \mathbf{v}]}{P[(\mathbf{\Lambda}, \mathbf{e})_\gamma | \mathbf{v}]}, 1\right], \quad (14a)$$

$$\text{else } (\mathbf{\Lambda}, \mathbf{e})_{\gamma+1} \leftarrow (\mathbf{\Lambda}, \mathbf{e})_\gamma. \quad (14b)$$

Eq. (14b) simply states that, in case of rejection of the trial model, the last accepted model is duplicated in the sequence and a new move in the parameter space is attempted from this point. With this method, the probability of the trial model  $P[(\mathbf{\Lambda}, \mathbf{e})_{\text{TRY}} | \mathbf{v}]$  is systematically compared to the previous model probability  $P[(\mathbf{\Lambda}, \mathbf{e})_\gamma | \mathbf{v}]$  by computing their ratio. Therefore non-normalized probabilities may be used to compute the denominator of eq. (7).

The annealing algorithm uses a control parameter,  $\zeta > 0$ , to obtain a deformed version of the posterior probability.

$$P_\zeta(\mathbf{\Lambda}, \mathbf{e} | \mathbf{v}) = \exp\left[\frac{\ln P(\mathbf{\Lambda}, \mathbf{e} | \mathbf{v})}{\zeta}\right]. \quad (15)$$

By varying  $\zeta$  from infinity to one,  $P_\zeta$  continuously goes from the uniform probability to the posterior probability. If  $\zeta$  is further decreased to zero, the probability density  $P_\zeta$  converges towards a Dirac distribution located on the model with the largest posterior probability.

$$P_{\zeta=0}(\mathbf{\Lambda}, \mathbf{e} | \mathbf{v}) = \delta[(\mathbf{\Lambda}, \mathbf{e}) - (\mathbf{\Lambda}, \mathbf{e})_{\text{BEST}}]. \quad (16)$$

This anamorphosis of the posterior probability is performed by decreasing  $\zeta$  while running the Metropolis algorithm so that the generated Markov Chain Monte Carlo sequence is progressively guided towards the region of the parameter space where  $P$  is maximum. It is important to note that this random walk will be successful only if the successive models forming the Markov chain are strongly correlated, that is, if  $(\mathbf{\Lambda}, \mathbf{e})_{\text{TRY}}$  only slightly differs from  $(\mathbf{\Lambda}, \mathbf{e})_\gamma$ .

#### 3.2 Implementation of the method

We now explain the details of the implementation of the Metropolis-annealing method to solve eq. (7) using the probability densities given in eqs (10a), (10b), (12c) and (13).

In the first stage of the Metropolis-annealing inversion  $\zeta$  is decreased down to a very small value, numerically equivalent to zero, to converge near  $(\mathbf{\Lambda}, \mathbf{e})_{\text{BEST}}$ , that is, the model with the largest posterior probability. During this stage, the posterior probability asymptotically converges towards the Dirac distribution of eq. (16). The absolute amplitude of the posterior probability is not important as long as the topology of  $P_\zeta(\mathbf{\Lambda}, \mathbf{e} | \mathbf{v})$  is preserved. Consequently, during this search for the best model, the posterior probability may be replaced, both in the Metropolis filtering and in the annealing anamorphosis, by any function

$$\vartheta_\zeta(\mathbf{\Lambda}, \mathbf{e} | \mathbf{v}) = \chi[P_\zeta(\mathbf{\Lambda}, \mathbf{e} | \mathbf{v})], \quad (17)$$

where  $\chi$  is any strictly monotonously increasing function defined in  $\mathbb{R}^+$ ,  $P_\zeta(\mathbf{\Lambda}, \mathbf{e} | \mathbf{v})$  has then to be strictly positive. This condition is satisfied when the values of the unknown parameters are restricted to  $\mathbf{\Lambda} > 0$  and  $\mathbf{e} \in [0, 1]$  as required by eqs (10a) and (10b). From eq. (9), this implies that the non-normalized value of  $P(\mathbf{\Lambda}, \mathbf{e})$  is a constant on the whole restricted domain. The prior constraints

represented by eqs (10a) and (10b) can then easily be satisfied by bounding the parameter space. Consequently, for any model belonging to this bounded space, the posterior probability of eq. (7) is given by either eq. (12c) or (13) depending on the value of the parameters.

Choosing  $\chi$  as the natural logarithm, eq. (15) becomes

$$\vartheta_{\zeta}(\Lambda, \mathbf{e} | \mathbf{v}) = \frac{\ln P(\Lambda, \mathbf{e} | \mathbf{v})}{\zeta}. \quad (18)$$

This equation gives

$$\begin{aligned} \vartheta_{\zeta}(\Lambda, \mathbf{e} | \mathbf{v}) = & \frac{1}{\zeta} \sum_{\alpha} \sum_{v_{i,j,k,l} \in \mathcal{N}_{\alpha}} (-\lambda_{\alpha,i,j,k,l} \\ & + \lambda_{\alpha,i,j,k,l} \ln v_{i,j,k,l} - \ln v_{i,j,k,l}!) \end{aligned} \quad (19)$$

for the probability density of eq. (12c), and

$$\begin{aligned} \vartheta_{\zeta}(\Lambda, \mathbf{e} | \mathbf{v}) = & -\frac{1}{\zeta} \sum_{\alpha} \sum_{v_{i,j,k,l} \in \mathcal{N}_{\alpha}} \left( \frac{(v_{i,j,k,l} - \lambda_{\alpha,i,j,k,l})^2}{2\lambda_{\alpha,i,j,k,l}} \right. \\ & \left. + 0.5 \ln(2\pi \lambda_{\alpha,i,j,k,l}) \right) \end{aligned} \quad (20)$$

for the probability density of eq. (13).

The use of  $\vartheta_{\zeta}$  instead of  $P_{\zeta}$  allows to both save a significant amount of computational time and to gain in numerical accuracy by avoiding to estimate products of exponentials with either very large or very small arguments.

At the end of the first stage of the algorithm, the Markov sequence is supposed to have converged, and the second stage can start to construct the posterior probability in the vicinity of  $(\Lambda, \mathbf{e})_{\text{BEST}}$ . In practice, this is done by initializing a new Markov Chain Monte Carlo sequence at  $(\Lambda, \mathbf{e})_{\text{BEST}}$ , running a Metropolis loop with  $\zeta = 1$  and using the actual posterior probability densities of eqs (12c) and (13). By this way, the so-obtained sequence models gives a large sampling of the posterior probability density (Mosegaard & Tarantola 1995). This sequence can be used to derive statistical quantities such as marginal probabilities.

## 4 SYNTHETIC EXAMPLES

### 4.1 Common detection direction constraint

We first discuss a synthetic example using a parametrization where the  $\lambda_{m,n}$  terms are defined for all directions as indicated in eq. (5). We simulate a synthetic data set,  $\{v_{i,j,k,l}\}$ , for a virtual telescope equipped with matrices of  $5 \times 5$  pixels and oriented towards the zenith. The efficiencies of the scintillator bars are uniformly drawn in the  $[0.8, 1]$  interval excepted for  $a_5^y = 0.3$  and  $b_3^z = 0.2$ , which simulate two deficient bars. The Poissonian parameters,  $\lambda_{m,n}$ , are taken equal to  $5 \times 10^3 \cos(\theta)$  with  $\theta$  the zenith angle to generate the  $n_{i,j,k,l}$  terms. The synthetic data,  $v_{i,j,k,l}$ , are obtained through eq. (4).

The annealing loop starts at  $\zeta = 10^5$  and stops at  $\zeta = 1$ , and the decrease of temperature at the end of iteration  $K$  is given by  $\zeta_{K+1} = 0.9\zeta_K$ . Each Metropolis sequence counts  $5 \times 10^3$  iterations. The efficiencies obtained at the end of the annealing normalized by their true values are shown in the top part of Fig. 5. In this figure, the relative efficiencies are ranked according to their geometrical arrangement, and the normalization emphasizes the presence of trends in the efficiency values. It can be observed that a trend for a given group of efficiencies (i.e. scintillator bars) is compensated by an opposite trend in the corresponding group of the other matrix.

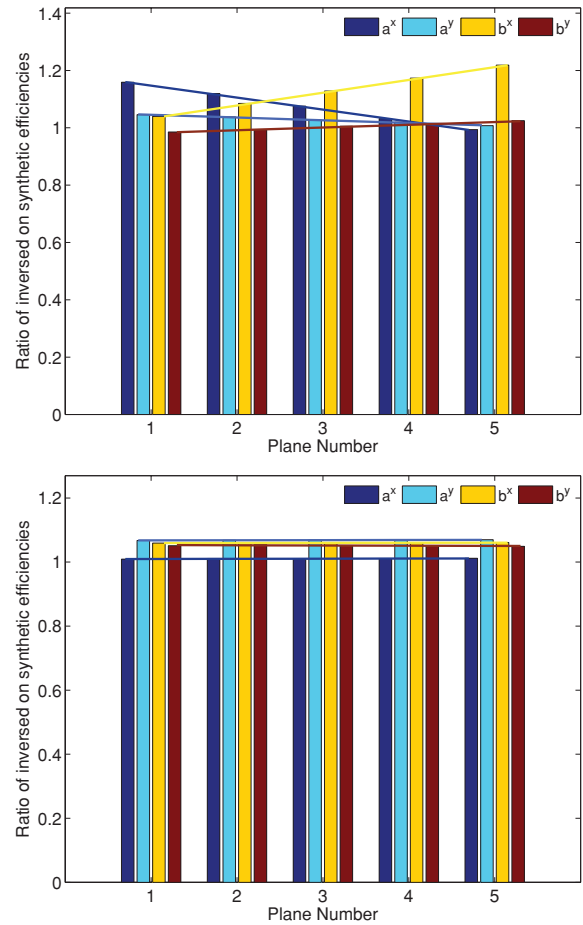


**Figure 5.** Top panel: relative efficiencies inverted under the common-direction constraint. Observe the linear trend bias affecting each family of parameters. Bottom: same as top for an inversion performed with the common-zenith angle constraint. The linear trend bias have disappeared, but constant-offset bias remain.

These trends are understandable by considering eq. (4) where the product of the  $(a^x, a^y, b^x, b^y)$  allows, for instance, a multiplicative bias  $\alpha^x$  in the  $a^x$  terms to be compensated by an opposite multiplicative bias  $\beta^x$  in the  $b^x$  terms. The bias must be such that,

$$\alpha^x a^x \times \beta^x b^x = a^x \times b^x. \quad (21)$$

This synthetic example shows that such compensations are left possible despite the coupling imposed by the common direction constraint represented by eq. (5). The trends belong to the null-space of the forward problem, making the inversion ill-posed and non-unique.

### 4.2 Common zenith angle constraint

We now consider a constraint which assigns a common  $\lambda_{\alpha}$  to all data sharing the same zenith angle as introduced in Section 2.1. This constraint exploit the circular symmetry of the open-sky integrated flux of muons around the vertical axis (Gaisser & Stanev 2008).

This symmetry assumption could eventually be questioned because of the east–west effect due to the geomagnetic field, which deviates the charged particles contained in the primary cosmic rays and makes the flux of particles coming from the west larger than from east (Grieder 2001; Dorman 2009). However, the east–west effect mainly concerns low-energy particles, which do not penetrate

deep in the atmosphere, and detailed models of air showers accounting for the geomagnetic field have shown that the east–west effect on the flux of muons is negligible at the ground level (Hansen *et al.* 2005). This could be no more valid for telescope data acquired on high-altitude volcanoes. A small anisotropy of the muon flux related to the anisotropic distribution of the Galactic sources also exists. However, this anisotropy is of the order of 0.05 per cent (e.g. fig. 2 of Munakata *et al.* 1997) and may safely be neglected in this study.

The common zenith angle constraint merges data from several directions and is tighter than the common-direction constraint discussed in the preceding section. It further reduces the number of  $\lambda_{\alpha}$  parameters and reinforces the coupling between the  $a$  and  $b$  efficiencies. By this way, it is supposed to limit the non-uniqueness and, hopefully, to eliminate the trends observed in the top part of Fig. 5. For the telescope with two matrices of  $5 \times 5$  pixels considered in the present synthetic example, the common-zenith angle constraint reduces the number of  $\lambda_{\alpha}$  from 81 to 12.

The relative inverted efficiencies are shown in the bottom part of Fig. 5. The most striking characteristic of the results is the disappearance of the trends observed in the first example performed with the common-direction constraint. All other inversions we performed with the common-zenith angle constraint also contained no trends. Although a formal demonstration remains to be done, this seems to indicate that the common-zenith angle constraint sufficiently couples the parameters to eliminate the null-space component represented by the multiplicative trends. However, a constant multiplicative bias remains. In the present example, the product of bias observed for the efficiencies amounts to 8 per cent compensated by an opposite 8 per cent bias on the  $\lambda_{\alpha}$  values.

## 5 INVERSION OF REAL DATA

We now turn to the inversion of the third data set of Table 1, which has been obtained for the telescope axis oriented at a zenith angle close to  $0^\circ$ . This vertical orientation of the telescope allows a full implementation of the common-zenith angle constraint. The number of events detected by each scintillator bar are given in Fig. 3. The telescope configuration, with two matrices of  $16 \times 16$  pixels, imposes 961 unknown  $\lambda_{m,n}$  and 64 efficiencies. By applying the common-zenith angle constraint, the number of  $\lambda_{\alpha}$  terms decreases to 43 giving 107 unknown parameters in total. In practice, this reduction of the number of parameters not only reduces the non-uniqueness of the inversion but also dramatically shrinks the parameter space and speeds up the annealing convergence. The values of the annealing parameters are identical to those used for the synthetic tests discussed earlier.

The inverted efficiencies are shown in the top part of Fig. 6. The failure of the  $b_{12}^y$  bar and, to a lesser extent, the one of  $b_3^x$  (both in the rear matrix) is confirmed as suspected by looking at the events distribution in Fig. 3. All inverted  $a^x$  efficiencies are lower than 1 and, because of the possible existence of a multiplicative constant bias, they could be multiplied by a constant factor to make  $\max(a^x) = 1$ . Of course, this arbitrary shift, must be compensated by a division of the  $\lambda_{\alpha}$  terms by the same factor. This possibility illustrates the fact that an absolute determination of both the flux (i.e. the  $\lambda_{\alpha}$  terms) and the acceptance (i.e. the  $a$  and  $b$  values) is impossible. The inverted Poissonian parameters,  $\lambda_{\alpha}$ , are shown in Fig. 7. The monotonous decrease expected as a function of the zenith angle is well reproduced.

The bottom part of Fig. 6 shows the number of events that would have been measured with bars having a 100 per cent efficiency.

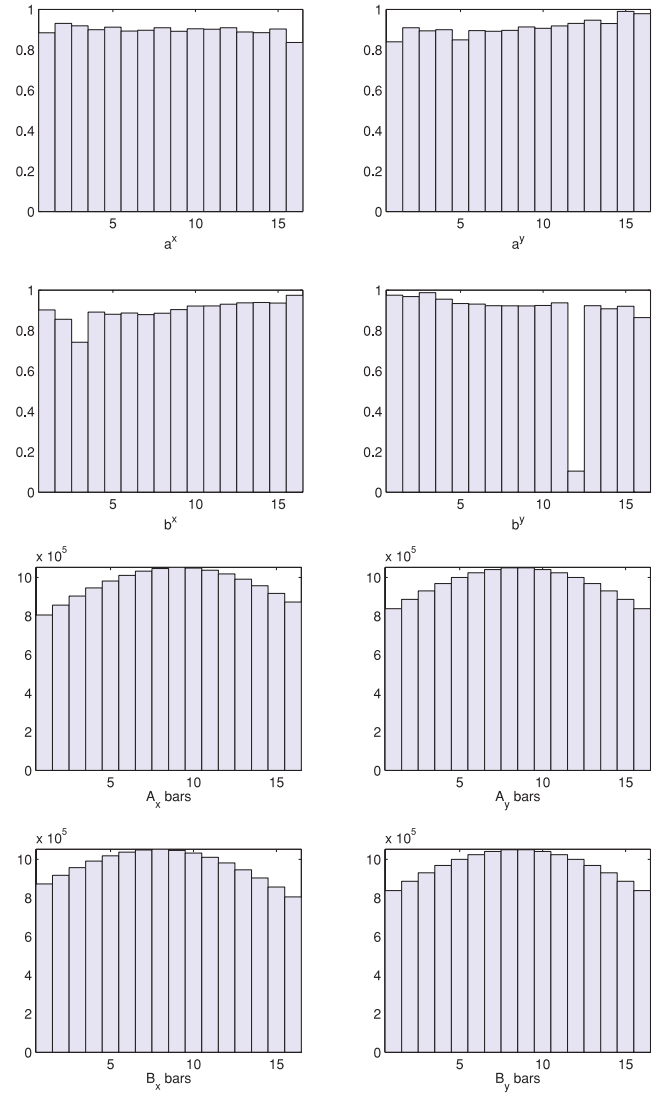


**Figure 6.** Top: inverted efficiencies for the third data set in Table 1. The  $a_{12}^y$  bar clearly fails due to a bad optical coupling of the scintillator bar. Bottom: reconstructed number of events for each scintillator bar obtained by correcting the measured number of events of Fig. 3 with the inverted efficiencies.

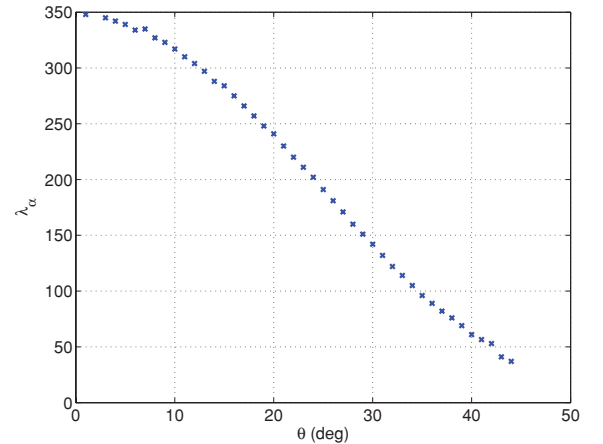


**Figure 7.** Inverted Poissonian parameters,  $\lambda_{\alpha}$ , as a function of the zenith angle.

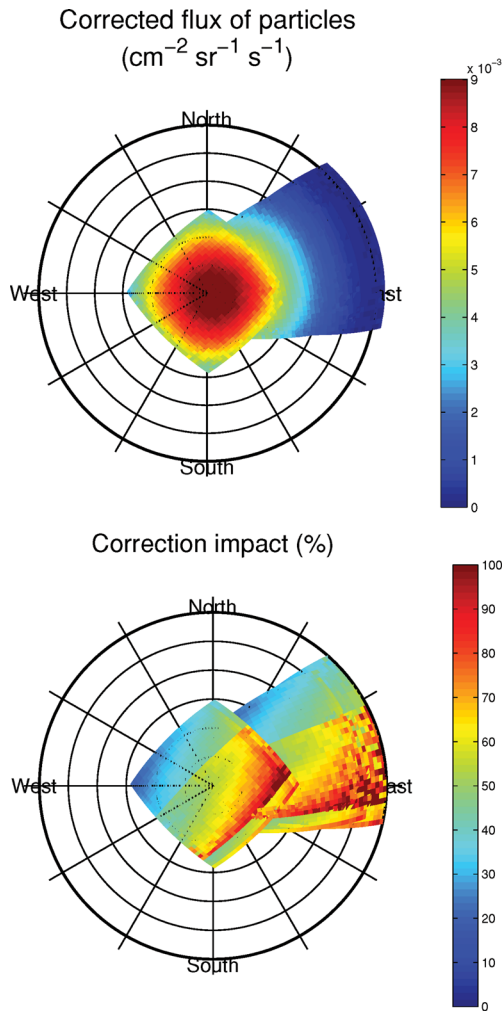


**Figure 8.** Top: detected particles flux, corrected with the efficiencies displayed in Fig. 6. Bottom: influence of the correction on the detected flux.

These numbers are obtained by dividing the number of events actually measured (Fig. 3) by the inverted efficiencies. The symmetrical distribution of event expected for a perfect telescope is recovered.

The inverted efficiencies of Fig. 6 can be used to derive a corrected acceptance,  $\mathcal{T}(\mathbf{r}_{m,n})$ , applied to the flux of Fig. 4 (top) corresponding to the three data sets of Table 1. The resulting undistorted flux is shown in the top part of Fig. 8, and the discrepancy between the measured flux and the undistorted flux is given in the bottom part of Fig. 8. The undistorted flux appears much more regular and symmetrical than the empirically corrected flux shown at the bottom of Fig. 4.

## 6 CONCLUDING REMARKS

Combining individual muon radiographies to perform the tomography inversion of the 3-D density distribution requires radiographies cleaned from spurious features due to defects of the telescope acceptance. Indeed, such artefacts may induce inconsistencies in the resulting linear system of equations leading to unpredictable reconstruction errors. Undistorting images from the telescope acceptance then constitute an important issue in the processing sequence of muon tomography. In this study, we implement a systematic method

to account for the actual acceptance function of scintillator-based muon telescopes where low efficiency and even failure of detection bars may produce spurious features in the measured flux.

Using the number,  $v_{i,j,k,l}$ , of detected events for each pair of pixels of the telescope matrices, the determination of the acceptance cannot be separated from the determination of the unknown number of events,  $n_{i,j,k,l} \geq v_{i,j,k,l}$ , which actually hit the bars. This duality is expressed in eq. (4) where the efficiencies,  $a_i^x$ ,  $a_j^y$ ,  $b_k^x$  and  $b_l^y$ , play the same role as  $n_{i,j,k,l}$ . A fundamental non-uniqueness results from this coupling, its main expression being that the efficiencies may be decreased by an arbitrary factor without changing the fit to the data provided the  $n$  values are increased by the same factor. Furthermore this unavoidable non-uniqueness increases generally because trend bias is present in the efficiencies. Such trends come from insufficient couplings among the parameters of the inverse problem. A possibility to overcome this consists in merging data with the same zenith angle as illustrated in Fig. 5. This requires either an open-sky data flux measured towards the zenith or several measurements with different orthogonal orientations of the detection matrices to couple the  $x$  and  $y$  efficiency coefficients.

Let us remark that the fundamental coupling of the parameters represented by eq. (5) supposes that the flux is the same for all pixel pairs sharing the same direction. This constraint may be defeated if the telescope is very near strong density heterogeneities as could occur, for instance, against the edge of a cliff with the matrices partly exposed to open sky. In such a particular case, the flux coming from a given direction will no more be the same for all pixel pairs, and the method discussed in this paper will fail.

The parametrization presented in Section 2.1 supposes that  $n_{i,j,k,l} \geq v_{i,j,k,l}$ . This assumption implies that events corresponding to fake tracks and the soft electronic component has properly been removed from the data set. This issue is discussed in details by Nagamine *et al.* (1995) and in the book (section 9.2.3) by Nagamine (2003) who recommend to use an iron shielding to filter out the soft component and a third detection matrix to make fortuitous coincidences highly unlikely by implementing a triple coincidence constraint. Our telescopes are equipped with these devices.

The simulated annealing algorithm used to implement the Bayesian inversion easily allows to eventually use more complicated models. This is for instance the case of the bar efficiencies, which are assumed constant in this study (eq. 4) and could instead account for an eventual along-fibre attenuation of light. This could be of some importance for large telescopes using scintillator bars with a length of several metres not negligible with respect to the attenuation length of the fibres. This is not the case for our telescopes whose scintillator bars have a length of 0.8 m.

The Bayesian formalism discussed in this paper also furnishes an inverted estimate of the number of muons  $n_{i,j,k,l}$ —some of them being undetected due to unperfect efficiencies—which actually crossed the telescope. In practice, these numbers are represented by the Poissonian hyperparameters,  $\lambda_\alpha$ , which are the quantities actually inverted (Fig. 7). The  $\lambda$  values represent the parameters of the Poissonian stochastic processes from which the  $n_{i,j,k,l}$  can be drawn. These stochastic processes then constitute the models for the flux of muon measured in the directions spanned by the telescope. As such, they form a stochastic model of the radiography from which other quantities like opacity and integrated density images may be derived (see Lesparre *et al.* 2010 for terminology) and subsequently be used for 3-D tomography inversion. Whenever open-sky data are available, the inversion of the  $\lambda$  terms can be further constrained by using prior model of muon flux as discussed by Lesparre *et al.* (2010).

## ACKNOWLEDGMENTS

This paper is dedicated to the memory of our friend and colleague Albert Tarantola who participated with us to the launch of the DIAPHANE muon tomography project and who inspired many ideas developed in this paper. We thank the reviewers for their constructive remarks, which improved the manuscript. The design and the construction of the telescopes greatly benefited from the skilled expertise of Bruno Carlus (computer), Bruno Kergosien (electronics), Pascal Rolland (mechanical engineering) and Sylvain Vanzetto (optical fibres). The DIAPHANE project is financially supported by the IGP (www.ipgp.fr) BQR grant, the DOMOSCAN ANR (www.agence-nationale-recherche.fr) project, the CNRS/IN2P3 (www.cnrs.fr) Astroparticles program and the MD experiment of the Mont Terri project (www.mont-terri.ch) funded by Swisstopo and CRIEPI partners. This is IGP contribution 3233.

## REFERENCES

- Alvarez, L.W. *et al.*, 1970. Search for hidden chambers in the pyramids, *Science*, **167**, 832–839.
- Barrett, P.H., Bollinger, L.M., Cocconi, G., Eisenberg, Y. & Greisen, K., 1952. Interpretation of cosmic-ray measurements far underground, *Rev. modern Phys.*, **24**, 133–178.
- Bhanot, G., 1988. The metropolis algorithm, *Rep. Prog. Phys.*, **51**, 429–457.
- Dorman, L.I., 2009. *Cosmic Rays in Magnetospheres of the Earth and Other Planets*, Springer, New York, NY.
- Gaisser, T. & Stanev, T., 2008. Cosmic rays, *Phys. Lett. B*, **667**, 254–260, doi:10.1016/j.physletb.2008.07.028.
- Gibert, D. & Le Mouél, J.L., 2008. Inversion of polar motion data: Chandler wobble, phase jumps, and geomagnetic jerks, *J. geophys. Res.*, **113**, B10405, doi:10.1029/2008JB005700.
- Gibert, D. & Virieux, J., 1991. Electromagnetic imaging and simulated annealing, *J. geophys. Res.*, **96**, 8057–8067.
- Gibert, D., Beauducel, F., Déclais, Y., Lesparre, N., Marteau, J., Nicollin, F. & Tarantola, A., 2010. Muon tomography: plans for observations in the Lesser Antilles, *Earth Planets Space*, **62**, 153–165.
- Grieder, P.K.F., 2001. *Cosmic Rays at Earth: Researcher's Reference Manual and Data Book*, Elsevier Science, Amsterdam.
- Hansen, P., Gaisser, T.K., Stanev, T. & Sciutto, S.J., 2005. Influence of the geomagnetic field and of the uncertainties in the primary spectrum on the development of the muon flux in the atmosphere, *Phys. Rev. D*, **71**, 083012, doi:10.1103/PhysRevD.71.083012.
- Kirkpatrick, S., Gelatt, C.D. & Vecchi, M.P., 1983. Optimization by simulated annealing, *Science*, **220**, 671–680.
- Lesparre, N., Gibert, D., Marteau, J., Déclais, Y., Carbone, D. & Galichet, E., 2010. Geophysical muon imaging: feasibility and limits, *Geophys. J. Int.*, **183**, 1348–1361.
- Marteau, J., Gibert, D., Lesparre, N., Nicollin, F., Noli, P. & Giacoppo, F., 2011. Muons tomography applied to geosciences and volcanology, *Nucl. Instr. Methods A*, in press.
- Metropolis, N., Rosenbluth, A., Rosenbluth, N., Teller, A. & Teller, E., 1953. Equation of the state calculations by fast computing machines, *J. Chem. Phys.*, **21**, 1087–1092.
- Mosegaard, K., & Tarantola, A., 1995. Monte-Carlo sampling of solutions of inverse problems, *J. geophys. Res.*, **100**, 12 431–12 447.
- Munakata, K. and the Kamiokande Collaboration, 1997. Large-scale anisotropy of the cosmic-ray muon flux in Kamiokande, *Phys. Rev. D*, **56**, 23–26.
- Nagamine, K., 1995. Geo-tomographic observation of inner-structure of volcano with cosmic-ray muons, *J. Geography*, **104**, 998–1007.
- Nagamine, K., 2003. *Introductory Muon Science*, Cambridge University Press, Cambridge, 208 pp.
- Nagamine, K., Iwasaki, M., Shimomura, K. & Ishida, K., 1995. Method of probing inner-structure of geophysical substance with the horizontal cosmic-ray muons and possible application to volcanic eruption prediction, *Nucl. Instr. Meth. A*, **356**, 585–595.
- Nicollin, F., Gibert, D., Lesparre, N. & Nussbaum, C., 2010. Anisotropy of electrical conductivity of the excavation damaged zone in the Mont Terri underground rock laboratory, *Geophys. J. Int.*, **181**, 303–320, doi: 10.1111/j.1365-246X.2010.04517.x.
- Papoulis, A. & Pillai, S.U., 2002. *Probability, Random Variables, and Stochastic Processes*, McGraw Hill Higher Education, New York, 852 pp.
- Pessel, M. & Gibert, D., 2003. Multiscale electrical impedance tomography, *J. geophys. Res.*, **108**, doi: 10.1029/2001JB000233.
- Tanaka, H. *et al.*, 2008. Radiographic imaging below a volcanic crater floor with cosmic-ray muons, *Am. J. Sci.*, **308**, 843–850.
- Tanaka, H., Uchida, T., Tanaka, M., Shinohara, H. & Taira, H., 2009a. Cosmic-ray muon imaging of magma in a conduit: degassing process of Satsuma Iwojima Volcano, Japan, *Geophys. Res. Lett.*, **36**, L01304, doi:10.1029/2008GL036451.
- Tanaka, H. *et al.*, 2009b. Detecting a mass change inside a volcano by cosmic-ray muon radiography (muography): first results from measurements at Asama volcano, Japan, *Geophys. Res. Lett.*, **36**, L17302, doi:10.1029/2009GL039448.
- Tarantola, A., 2005. *Inverse Problem Theory and Methods for Model Parameter Estimation*, Society for Industrial and Applied Mathematics, Philadelphia, 342 pp.